NANO LETTERS

pubs.acs.org/NanoLett Letter

Spin-State-Selective Excitation in Spin Defects of Hexagonal Boron Nitride

Mohammad Abdullah Sadi,* Luca Basso, David A. Fehr, Xingyu Gao, Sumukh Vaidya, Emmeline G. Riendeau, Gajadhar Joshi, Tongcang Li, Michael E. Flatté, Andrew M. Mounce,* and Yong P. Chen*

Cite This: *Nano Lett.* 2025, 25, 12067−12074 Read Online

ABSTRACT: Hexagonal boron nitride (hBN) has emerged as a promising two-dimensional platform for quantum sensing due to its optically addressable spin defects, such as the negatively charged boron vacancy (V_B^-). Spectral overlap of spin transitions due to large hyperfine interactions has limited its magnetic sensitivity. Here, we demonstrate spin-selective excitation of V_B^- spin defects in hBN driven by a circularly polarized microwave. Using a cross-shaped microwave resonance waveguide, we superimpose two orthogonally linearly polarized microwaves shifted in phase from an FPGA to generate circularly polarized microwaves. This enables selective spin $|0\rangle \rightarrow |-1\rangle$ or $|0\rangle \rightarrow |1\rangle$ excitation of V_B^- defects, as confirmed by optically detected magnetic resonance experimentally and supported computationally. We also investigate the influence of the magnetic field on spin-state selectivity. Our technique enhances the hBN platform for quantum sensing through better spin state control and magnetic sensitivity at low and zero fields.

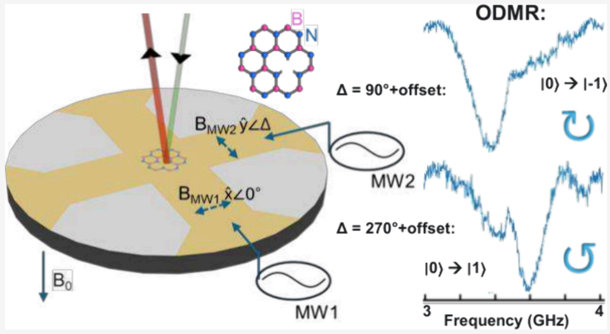

KEYWORDS: *quantum sensing, hexagonal boron nitride, spin defects, microwave polarization, spin-state control*

Quantum sensing technologies have seen remarkable advancements in recent years, with solid-state spin defects emerging as particularly promising platforms.[1−4] While nitrogen-vacancy (NV) centers in diamond have been widely studied, their applications are limited by challenges in fabrication, integration, and achieving close proximity to samples of interest.[5,6]

In this context, two-dimensional van der Waals materials, particularly hexagonal boron nitride (hBN), have garnered significant attention.[7−10] hBN's layered structure allows for exfoliation and direct transfer onto a wide variety of samples, enabling better proximity for quantum sensing. This capability, combined with hBN's wide bandgap and exceptional stability, positions it as a compelling platform for quantum sensing and information applications.[11−14] The negatively charged boron vacancy (V_B^-) in hBN, an optically addressable spin defect, was first identified in 2020.[15] Subsequent theoretical studies[16−18] and optically detected magnetic resonance (ODMR) experiments[19−22] have elucidated its atomic and electronic structure. The V_B^- defect is formed by a vacant boron site surrounded by three nitrogen atoms in the hBN lattice (Figure 1(b)). As illustrated in the energy level diagram in Figure 1(c), this defect possesses a spin-1 ground state and is optically addressable at room temperature, contributing to its suitability for quantum sensing applications.

Despite these promising characteristics, the potential of V_B^- defects for quantum sensing has been constrained by large hyperfine interactions. These interactions lead to broad ODMR with spectrally overlapped hyperfine spin transitions, especially at low magnetic fields, posing challenges for achieving high magnetic sensitivity. Overcoming this limitation is crucial for fully leveraging the sensing capabilities and applicability of hBN-based quantum sensors.

Circularly polarized microwave delivery devices have enabled significant advances in NV center manipulation, with early work demonstrating polarization-selective excitation and establishing the potential for operation down to zero magnetic field.[23] Technical developments have employed various design approaches, including frequency-tunable resonators,[24] microstrip circuits,[25] planar resonators with varactor diodes,[26] annular microstrip-line resonators,[27] and dielectric resonator antennas.[28] These advances have enabled practical applications such as zero-field magnetometry in NV systems using

Received: June 10, 2025
Revised: July 15, 2025
Accepted: July 17, 2025
Published: July 25, 2025

https://doi.org/10.1021/acs.nanolett.5c03056
Nano Lett. 2025, 25, 12067−12074

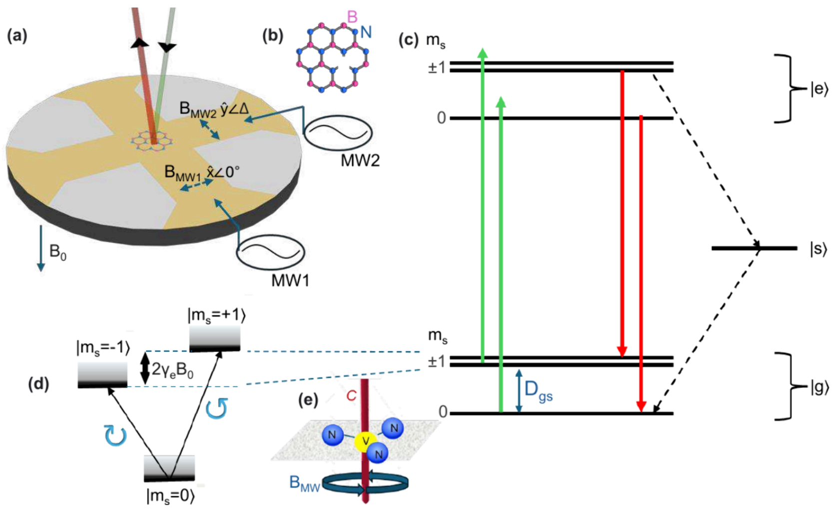

Figure 1. Experimental configuration, energy levels, and mechanism of spin-state selective excitation in V_B^- defects in hBN. (a) Gold on a sapphire device generating circularly polarized microwaves through superposition of orthogonal linearly polarized fields. Center: multilayer hBN containing spin defects. (b) Lattice structure of hBN with V_B^-. (c) Electronic energy level diagram of V_B^- showing $S = 1$ triplet states and an $S = 0$ metastable state mediating ODMR (green: optical excitation; red: radiative decay). |e⟩, |s⟩, and |g⟩ represent excited, metastable, and ground states. (d) Ground-state energy levels showing selective spin-state excitation via angular momentum transfer from circularly polarized microwaves. (e) The boron vacancy is symmetric along the *c*-axis of hBN, necessitating orthogonal circularly polarized microwaves as generated by the device in (a) to drive the spin-selective transition in (d).

polarization-selective microwave excitation.[29] Recent studies have also revealed cross-relaxation effects in NV systems occurring at zero magnetic field.[30,31] As conventional spectroscopic approaches are limited by spectral overlap of degenerate spin states at zero field, applying circular microwave polarization would be crucial for paving the way for investigation of zero-field magnetometry and cross-relaxation in V_B^- defects in hBN, as well as addressing the challenges posed by hyperfine broadening to enhance the system's sensing capabilities.

In this study, we explore the use of circularly polarized microwaves for spin-state selective excitation in V_B^- defects. We generated these defects through irradiation of hBN flakes with 2.5 keV He^+ ions. We employ a cross-shaped microwave waveguide and dual microwave signals with controlled phase difference generated from a field programmable gate array (FPGA) operated with the QICK-DAWG package[32] to create polarization-tunable microwave fields for spin manipulation (Figure 1(a)). We also investigated the influence of magnetic field strength on spin-state selectivity. Our work demonstrates spin-state selective excitation in V_B^- spin defects of hBN, addressing the challenge of spectral overlap caused by large hyperfine interactions. Our approach enables more control over spin state transitions, which is valuable for advancing hBN-based quantum sensing applications. This improved spin-state transition manipulation technique, combined with hBN's inherent advantages as a 2D platform, represents a significant step toward realizing high-resolution quantum sensing, with implications for nanoscale magnetic field detection, quantum information processing, and sensing applications in areas such as material science and biology.

The behavior of V_B^- defects in hBN is governed by the ground-state electron spin Hamiltonian, H_{gs}, which encompasses terms associated with zero field splitting (ZFS), electron Zeeman splitting, and electron−nuclear spin hyperfine interaction:[15,33]

$$H_{gs} = D_{gs}\left[S_z^2 - \frac{S(S+1)}{3}\right] + E_{gs}(S_x^2 - S_y^2) + \gamma_e \mathbf{B}\cdot\mathbf{S} + \sum_{k=1,2,3} \mathbf{S}\cdot\overline{\overline{A}}_k\cdot\mathbf{I}_k \quad (1)$$

Here, D_{gs} ($\approx h \times 3.48$ GHz) is the ground-state longitudinal ZFS parameter, E_{gs} ($\approx h \times 50$ MHz) is the transverse ZFS parameter, $S = 1$ is the electron spin quantum number, while S_z, S_x, and S_y are the corresponding spin operator components for a spin-1 system, γ_e is the electron-spin gyromagnetic ratio (with Landé g-factor $g = 2$, $\gamma_e = g\frac{e}{2m_e\hbar}$, where e is electron charge and m_e is electron mass), and $\mathbf{I}_k$ is the nuclear spin-1 vector operator of the three nearest ^{14}N nuclei[15] indexed by **k**. The hyperfine interaction tensor $\overline{\overline{A}}_k$ has a magnitude of approximately $h \times 47$ MHz.[15,18,34]

When an external magnetic field B_0 is applied perpendicular to the hBN plane, the resonant frequencies for transitions between the $m_s = 0$ and $m_s = \pm1$ states are given by

$$f_\pm = D_{gs}/h \pm \sqrt{E_{gs}^2 + (\gamma_e B_0)^2}\,/h \quad (2)$$

As illustrated in Figure 1(c), circularly polarized microwave radiation can selectively drive either the $m_s = 0 \rightarrow m_s = 1$ or $m_s = 0 \rightarrow m_s = -1$ transition depending on its handedness. This selectivity arises from angular momentum conservation rules.

To achieve this selective excitation, we implemented a cross-shaped microwave waveguide that generates circularly polarized microwaves. At the center of the cross, the magnetic field from the microwave is described by

$$\vec{B}_{MW} = B_{MW1}\hat{x}\sin(\omega t) + B_{MW2}\hat{y}\sin(\omega t + \Delta) \quad (3)$$

where Δ is the phase difference between the two orthogonal components, $\omega = 2\pi f$ is the angular frequency of the microwave (with f being the frequency), B_{MW1} and B_{MW2} are the amplitudes of the magnetic fields from orthogonally linearly polarized microwaves incoming at the center of the

https://doi.org/10.1021/acs.nanolett.5c03056
Nano Lett. 2025, 25, 12067−12074

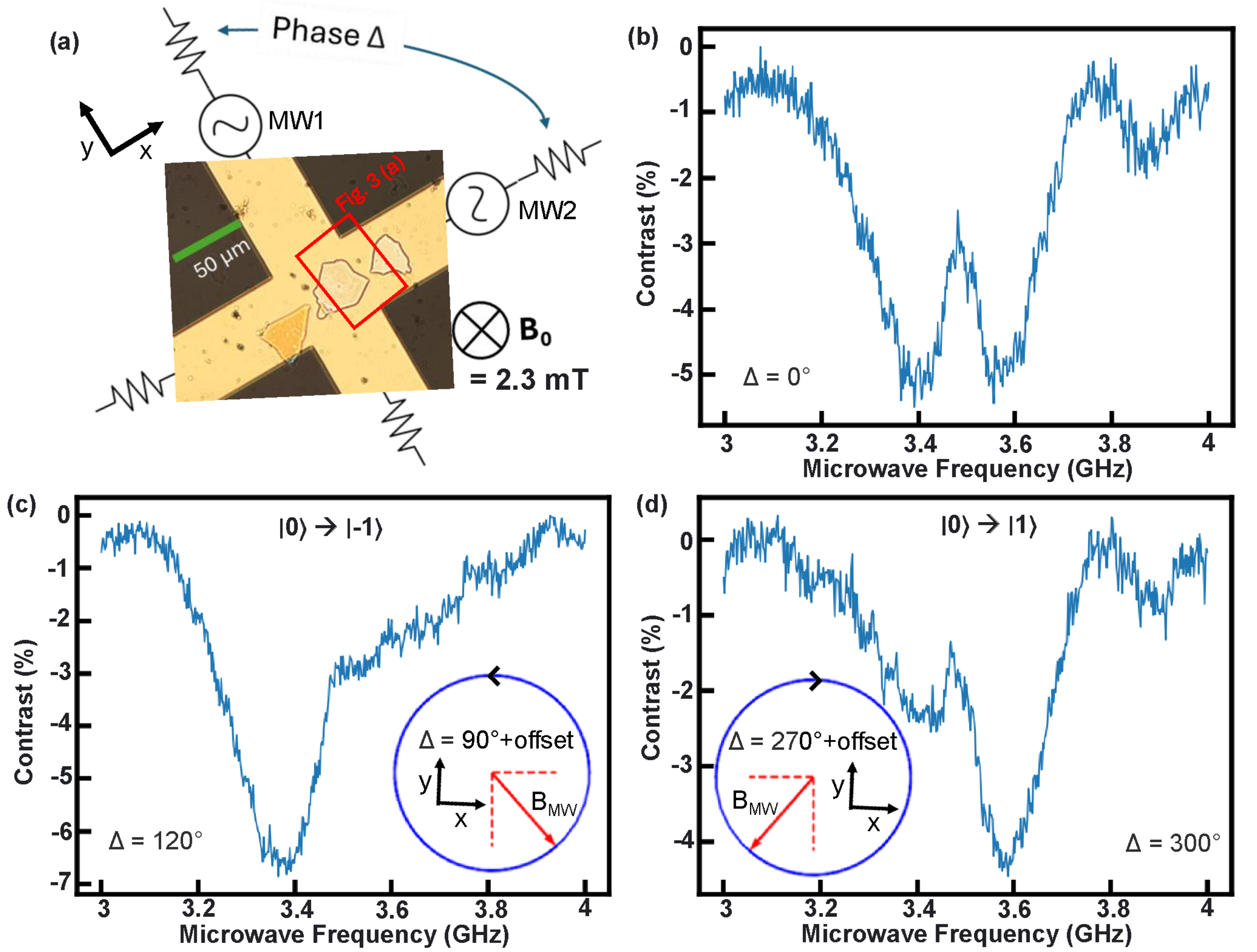

Figure 2. ODMR spectroscopy of V_B^- defects in hBN under controlled microwave polarization. (a) Optical image of orthogonal transmission lines (waveguides) carrying linearly polarized microwaves with controlled phase difference Δ, with an hBN flake at the intersection, under a magnetic field of 2.3 mT applied perpendicular to the surface. (b) ODMR spectrum with Δ = 0° applied (near linear microwave polarization). (c) ODMR spectrum at Δ = 120° (effectively 90°, thus counterclockwise circular polarization) showing selective |0⟩ to |−1⟩ excitation. (d) ODMR spectrum at Δ = 300° (effectively 270°, thus clockwise circular polarization), showing mostly selective |0⟩ to |1⟩ excitation.

cross, and t is time (see Figure 1(a)). We ensured approximately equal amplitudes between the orthogonal magnetic fields B_{MW1} and B_{MW2} by adjusting the power to obtain reasonably equivalent ODMR signal intensities when independently exciting the hBN flake through each arm of the cross waveguide. The equation then describes circular polarization when Δ = 90° or Δ = 270°, linear polarization when Δ = 0° or Δ = 180°, and elliptical polarization for other angles (modulo 360°). The x−y plane is perpendicular to the symmetry axis "c" of the defect shown in Figure 1(e).

Our experiments employ continuous wave (CW) ODMR measurements with contrast determined by the normalized relative photoluminescence change when the microwave drive is turned on. We used 532 nm laser excitation and collected emitted light at wavelengths above 630 nm. The complete optical setup details are provided in the Supporting Information (SP). The ODMR transition pathway, shown in Figure 1(c), illustrates the reduction of photoluminescence due to metastable state-mediated phonon transitions (nonradiative decays) when optically excited from $m_s = \pm 1$ compared to that from the $m_s = 0$ state, whereas the former can be reached from the $m_s = 0$ ground state under microwave at resonant frequencies. The cross waveguide design is a modification of previous gapped waveguides,[23] adapted for the V_B^- hBN platform. Unlike the previous capacitively coupled design[23] with sharp resonance, our modified version incorporates a directly coupled broadband waveguide (Figure 1(a) and Supporting Information). This adaptation addresses two key challenges: the broad ODMR signal of V_B^- defects and the difficulty in precisely tuning resonant frequencies.

To demonstrate spin-state selectivity in V_B^- defects, we transferred an hBN flake containing these defects to the center of our cross-shaped microwave waveguide, as shown in Figure 2(a). This configuration allows for the superposition of orthogonal microwave fields with adjustable phase differences. While ideally the superimposed microwaves should have equal strength, the different paths taken by the signals necessitated some adjustment of the input microwave magnitudes. We applied a perpendicular magnetic field of 2.3 mT to the flake using a permanent magnet and utilized 50 Ω terminations to minimize microwave reflections. ODMR spectra collected under these conditions are presented after the linear background subtraction. All measurements were performed at room temperature under ambient conditions.

https://doi.org/10.1021/acs.nanolett.5c03056
Nano Lett. 2025, 25, 12067−12074

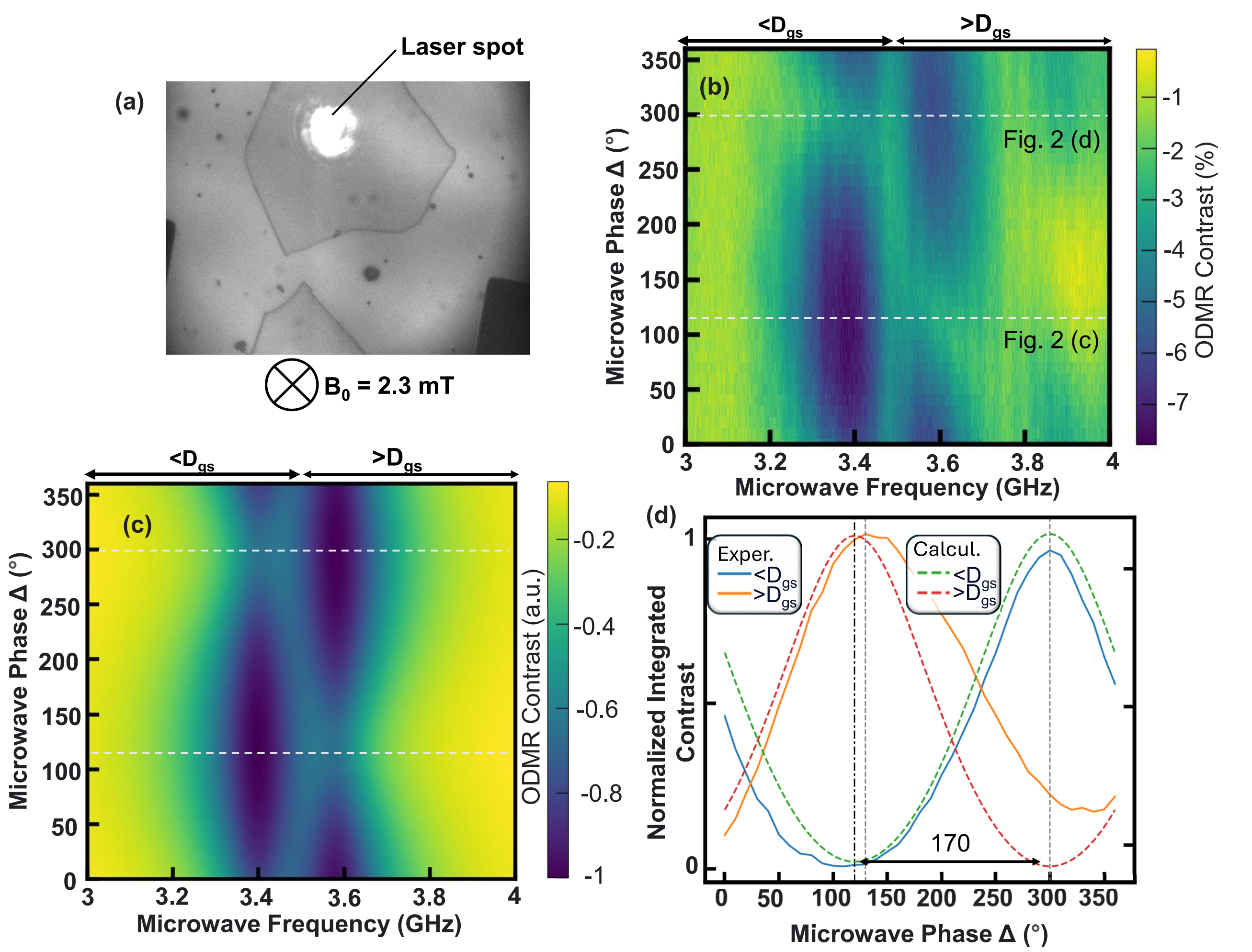

Figure 3. Continuous microwave phase-dependent ODMR modulation of V_B^- defects in hBN. (a) Optical image showing the laser spot for ODMR measurement. (b) Color plot of ODMR spectra evolution versus phase difference (Δ°) between orthogonal linearly polarized microwaves. (c) Corresponding Lindblad calculations of the spectral evolution. White dashed lines in both (b) and (c) mark maximum spin selectivities. (d) Normalized integrated contrast for frequencies below $D_{gs}(|0\rangle \rightarrow |-1\rangle)$ and above $D_{gs}(|0\rangle \rightarrow |1\rangle)$ with solid (dashed) lines depicting experimental (calculation) results.

Figure 2(b) presents the measured ODMR spectrum with zero applied phase difference (Δ = 0°) between the orthogonal microwave fields. The observed spectrum exhibits two resonance dips of nearly equal magnitude, indicating close to linearly polarized microwave excitation. However, due to differences in the microwave signal path lengths, some undetermined offset between the applied and actual phase difference may be present. As we varied the phase difference, we observed optimal spin selectivity for the $|0\rangle \rightarrow |-1\rangle$ transition at Δ = 120° (Figure 2(c)) and for the spin $|0\rangle \rightarrow |1\rangle$ transition at Δ = 300° (Figure 2(d)). This 180° separation in optimal phase differences aligns with our expectations based on eq 3 (90° and 270°), confirming the successful implementation of circularly polarized microwave excitation.

For this experiment, the offset phase between the applied and actual phase difference of the orthogonal microwaves comes out to be −30°. Thus, at Δ = 0°, the polarization of microwaves at the cross is slightly but not significantly deviated from being linear. Interestingly, the spin-state selectivity exhibits an asymmetry not observed in NV centers in diamond. Lorentzian fitting of the ODMR spectra, by which selectivity is defined as discussed in detail later in the discussion of Figure 4, reveals that the best-case scenario for the spin $|0\rangle \rightarrow |-1\rangle$ transition achieves 79.5 ± 1.7% selectivity, while the spin $|0\rangle \rightarrow |1\rangle$ transition reaches 67.4 ± 1.9% optimal selectivity. This asymmetry suggests an intrinsic difference between these transitions in V_B^- defects, which warrants further investigation. It is worth noting that the spurious peak around 3900 MHz observed in the ODMR data in Figure 2 likely arises from an aliasing artifact from the FPGA sampling process. This artifact does not affect the overall interpretation of our results but highlights the importance of considering potential experimental limitations in high-frequency measurements.

To gain a more comprehensive understanding of the spin-state selective excitation in V_B^- hBN, we investigate the continuous modulation of the transitions as a function of the microwave phase difference Δ. Figure 3(a) presents a magnified view of the experimental setup shown in Figure 2(a), clearly illustrating the laser spot with a diameter of 20 μm, at the center of the cross, on an hBN flake approximately 50 nm thick. The color plot in Figure 3(b) depicts the evolution in ODMR peak intensities as the phase between the orthogonal microwave fields is continuously tuned, with the

https://doi.org/10.1021/acs.nanolett.5c03056
Nano Lett. 2025, 25, 12067−12074

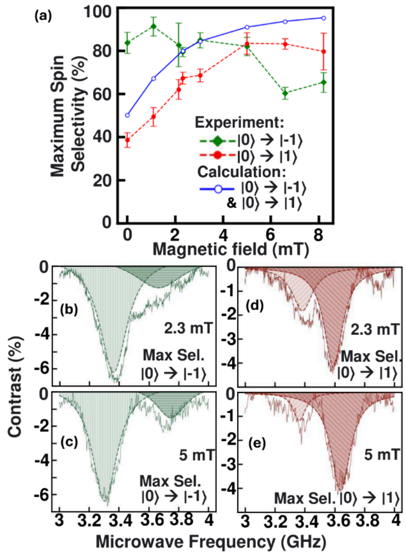

Figure 4. Magnetic field dependence of spin-state selectivity in V_B^- defects in hBN. (a) Maximum spin selectivity versus magnetic field showing experimental data for $|0\rangle \rightarrow |-1\rangle$ (green diamonds) and $|0\rangle \rightarrow |1\rangle$ (red circles) transitions with corresponding calculations (blue circles). (b−e) ODMR spectra at maximum selectivity for the $|0\rangle \rightarrow |-1\rangle$ transition of 2.3 mT (b) and 5 mT (c) and for the $|0\rangle \rightarrow |1\rangle$ transition at 2.3 mT (d) and 5 mT (e), each showing experimental data and light (dark) shaded area representing fitted Lorentzian to the $|0\rangle \rightarrow |-1\rangle$ ($|0\rangle \rightarrow |1\rangle$) component of the transition.

white dashed lines corresponding to the maximally selective transitions highlighted in Figure 2.

To corroborate the experimental data, simulations of ODMR were completed using the Lindblad formalism,[35−38] implemented using a combination of Mathematica software and the QuTiP Python package. Coherent transitions resulting from microwave-induced Rabi driving were modeled with a Hamiltonian of a similar form to eq 1, and the optical dynamics in Figure 1 were modeled with Lindblad jump operators and associated optical pumping and relaxation rates.[39] In the Hamiltonian, we used g = 2.002, D_{gs} = 3.49 GHz, and E_{gs} = 65 MHz, with parameters extracted from the fitting experimental data. The E_{gs} value reflects minor deviation from ideal C_{3v} symmetry of the defects under experimental conditions due to local structural or electronic environment asymmetries. A dephasing Lindblad jump operator was used to model finite temperature and hyperfine broadening effects on the ODMR line widths to match the measurements, with a dephasing rate of ∼100 μs^{-1}. In the simulation, a 7-level energy diagram was used, reflecting the S = 1, S = 1, and S = 0 spin character of the respective ground, excited, and metastable spin manifolds. Further details on the Lindblad calculations are provided in the Supporting Information. Figure 3(c) presents the corresponding Lindblad calculations of the spectral evolution observed in 3(b), with an offset phase of −30° incorporated. The calculations are in good agreement with the experimental data, as in both cases the white dashed lines representing maximum spin selectivities are separated by 180°.

By analyzing the data from Figures 3(b) and 3(c), the ODMR signal above and below the zero-field splitting frequency (D_{gs} = 3.49 GHz) is separated. The integrated ODMR contrast for these two frequency windows, plotted in Figure 3(d), demonstrates the continuous modulation of the spin-state selectivity. For both experimental and calculated results, we normalize the data such that the minimum value in each pair of data sets corresponds to zero and the maximum value corresponds to one. The solid lines represent the normalized experimental data, while the dashed lines show the normalized calculated values. The separation between phases corresponding to peaks in normalized integrated contrast for frequencies below D_{gs} (predominantly associated with $|0\rangle \rightarrow |-1\rangle$ transition) and above D_{gs} (predominantly associated with $|0\rangle \rightarrow |1\rangle$ transition) is approximately 170° in experimental data, while it is precisely 180° in the calculated results. This separation has good agreement with the expected phase difference of opposite circular polarizations, generated by the microwave fields as described in eq 3, each of which is expected to result in maximum selectivity for one of the spin-state transitions in the spin defects.

We investigate the dependence of spin-state selectivity in V_B^- defects on the magnetic field strength. By varying the applied magnetic field by varying the separation between the permanent magnet and the sample and sweeping the microwave phase difference Δ at each field strength, we characterized the maximum achievable spin-state selectivity for each transition. Average ODMR peak separation is used to characterize the magnitude of the magnetic field. Figure 4 presents the maximum selectivities as functions of the magnetic field. To quantify, the selectivity is defined for each of the two transitions for any ODMR spectrum by fitting Lorentzian functions to the ODMR peaks, as shown in Figure 4(b−e), and calculating the ratio of the area (light or dark, for $|0\rangle \rightarrow |-1\rangle$ and for $|0\rangle \rightarrow |1\rangle$, respectively) of the Lorentzian compared to the total fitted area (dark and light combined). Lorentzian fits were obtained using Origin software's double Lorentzian fitting routine applied on the spectra. The error bars represent the uncertainty in area calculations derived from the Lorentzian fitting. We also plot Lindblad calculation results (solid lines corresponding to the experimental data in dashed lines) in Figure 4(a).

Lindblad calculations do not exhibit differences in maximum selectivities between the $|0\rangle \rightarrow |1\rangle$ and $|0\rangle \rightarrow |-1\rangle$ transitions. However, experimental results reveal distinctly different behavior for the $|0\rangle \rightarrow |-1\rangle$ transition compared to that for the $|0\rangle \rightarrow |1\rangle$ transition. Maximum spin-state selectivity is generally robust across the examined magnetic field range for the $|0\rangle \rightarrow |-1\rangle$ transition, with the highest selectivity achieved reaching 91.4 ± 1.7 % at 1.1 mT. It is generally insensitive to the magnetic field below 5 mT, while decreasing to approximately 60% at the higher magnetic fields measured.

For both Lindblad calculations and experimental data for the maximum selectivity of the $|0\rangle \rightarrow |1\rangle$ transition, maximum selectivity increases with magnetic field and eventually tends to plateau. The experimental maximum selectivity of $|0\rangle \rightarrow |1\rangle$ is relatively poor at low magnetic field, but ultimately reaches 83.5 ± 1.9% at 5 mT. This behavior in V_B^- defects contrasts with that observed in NV^- centers in diamond subjected to a circularly polarized microwave. There, selectivity decreases with increasing magnetic field due to magnetic coupling between NV centers with different crystallographic orientations.[25] In the case of spin defects which all share the same crystallographic orientation in V_B^- hBN, higher magnetic field strengths reduce mixing between $|0\rangle \rightarrow |-1\rangle$ and $|0\rangle \rightarrow |1\rangle$ transitions, as demonstrated in Figure 4(d,e). At 5 mT (Figure 4(e)), the ODMR signals show lessened overlap between transitions compared to the 2.3 mT case (Figure 4(d)), which exhibits greater overlap and consequently lower selectivity.

https://doi.org/10.1021/acs.nanolett.5c03056
Nano Lett. 2025, 25, 12067−12074

However, the magnetic field (in)dependence and the robustness of selectivity for the $|0\rangle \rightarrow |-1\rangle$ transition across varied magnetic fields are not captured in our numerical model. Possible sources of this discrepancy and the differences in contrast obtained for maximum selectivities for the $|0\rangle \rightarrow |-1\rangle$ transition compared to the $|0\rangle \rightarrow |1\rangle$ transition as exemplified in Figure 2(c) and (d) may include in-plane electric fields entering into the Hamiltonian as $d_{\perp}$ or d' terms[37] or a small difference in the intersystem crossing rates from $|e, \pm1\rangle \rightarrow |s\rangle$ or $|s\rangle \rightarrow |g, \pm1\rangle$. Elucidating this discrepancy is the focus of future work.

In conclusion, we have demonstrated spin-state selective excitation in V_B^- defects in hBN using circularly polarized microwaves generated by a cross-shaped broadband waveguide. This approach expands the usefulness of the V_B^- hBN platform for low magnetic field sensing, quantum information applications, zero field magnetometry, and zero field cross-relaxation studies. Our experimental results, largely supported by Lindblad calculations, show continuous modulation of spin-state selectivity as a function of the phase difference between orthogonal microwave fields. Notably, an asymmetry in the maximum achievable selectivity was observed between the $|0\rangle \rightarrow |-1\rangle$ and $|0\rangle \rightarrow |1\rangle$ transitions, with the former exhibiting robustness across the tested magnetic field range and the latter showing improved selectivity at higher magnetic fields. The improved selectivity for the higher energy $|0\rangle \rightarrow |1\rangle$ transition at higher magnetic fields can be attributed to reduced mixing between the two transitions, as demonstrated by the lessened overlap in the ODMR signals. This behavior contrasts with that observed in NV^- centers in diamond, where selectivity decreases with increasing magnetic field due to interactions between differently oriented defects. These findings demonstrate the potential of V_B^- defects in hBN for applications requiring spin-state selectivity. Further investigations are necessary to fully understand the underlying physics of the selectivity behaviors of V_B^- not captured by the Lindblad model, such as the asymmetry observed between the selectivities of the two transitions and the robustness of selectivity for the $|0\rangle \rightarrow |-1\rangle$ over a range of magnetic fields.

■ ASSOCIATED CONTENT

Supporting Information

The Supporting Information is available free of charge at https://pubs.acs.org/doi/10.1021/acs.nanolett.5c03056.

> Experimental methods (sample preparation, waveguide fabrication, optical and microwave instrumentation), Lindblad model implementation, magnetic sensitivity analysis for circularly polarized excitation, magnetic field-dependent phase difference analyses (PDF)

■ AUTHOR INFORMATION

Corresponding Authors

Mohammad Abdullah Sadi − *Elmore Family School of Electrical and Computer Engineering and Department of Physics and Astronomy, Purdue University, West Lafayette, Indiana 47907, United States;* orcid.org/0009-0009-5769-7068; Email: msadi@purdue.edu

Andrew M. Mounce − *Center for Integrated Nanotechnologies, Sandia National Laboratories, Albuquerque, New Mexico 87123, United States;* orcid.org/0000-0002-8115-2764; Email: amounce@sandia.gov

Yong P. Chen − *Elmore Family School of Electrical and Computer Engineering, Department of Physics and Astronomy, Birck Nanotechnology Center, and Purdue Quantum Science and Engineering Institute, Purdue University, West Lafayette, Indiana 47907, United States;* Email: yongchen@purdue.edu

Authors

Luca Basso − *Center for Integrated Nanotechnologies, Sandia National Laboratories, Albuquerque, New Mexico 87123, United States;* orcid.org/0000-0002-7941-9976

David A. Fehr − *Department of Physics and Astronomy, University of Iowa, Iowa City, Iowa 52242, United States;* orcid.org/0009-0002-9103-0178

Xingyu Gao − *Department of Physics and Astronomy, Purdue University, West Lafayette, Indiana 47907, United States;* orcid.org/0000-0003-1253-4811

Sumukh Vaidya − *Department of Physics and Astronomy, Purdue University, West Lafayette, Indiana 47907, United States;* orcid.org/0000-0002-9732-6829

Emmeline G. Riendeau − *Center for Integrated Nanotechnologies, Sandia National Laboratories, Albuquerque, New Mexico 87123, United States; Department of Physics, University of Chicago, Chicago, Illinois 60637, United States*

Gajadhar Joshi − *Center for Integrated Nanotechnologies, Sandia National Laboratories, Albuquerque, New Mexico 87123, United States*

Tongcang Li − *Department of Physics and Astronomy, Elmore Family School of Electrical and Computer Engineering, Birck Nanotechnology Center, and Purdue Quantum Science and Engineering Institute, Purdue University, West Lafayette, Indiana 47907, United States;* orcid.org/0000-0003-3308-8718

Michael E. Flatté − *Department of Physics and Astronomy, University of Iowa, Iowa City, Iowa 52242, United States;* orcid.org/0000-0001-5093-1549

Complete contact information is available at: https://pubs.acs.org/10.1021/acs.nanolett.5c03056

Notes

The authors declare no competing financial interest.

■ ACKNOWLEDGMENTS

We thank the U.S. Department of Energy, Office of Science, National Quantum Information Science Research Centers, and Quantum Science Center for support through contract DE-AC05-00OR22725 for experimental work at Purdue University. This work was also funded, in part, by the Laboratory Directed Research and Development Program and performed, in part, at the Center for Integrated Nanotechnologies, an Office of Science User Facility operated for the U.S. Department of Energy (DOE) Office of Science. Sandia National Laboratories is a multimission laboratory managed and operated by National Technology and Engineering Solutions of Sandia, LLC, a wholly owned subsidiary of Honeywell International, Inc., for the DOE's National Nuclear Security Administration under contract DE-NA0003525. The calculation results are based upon work supported by the Air Force Office of Scientific Research under award number FA9550-22-1-0308. This paper describes objective technical results and analysis. Any subjective views or opinions that might be expressed in the paper do not necessarily represent the views of the U.S. Department of Energy or the United States Government. We also thank Dr. Aroop Behera for assistance with 2D material transfer logistics, Dr. Sho Uemura for assistance with FPGA firmware, and Dr. Pauli Kehayias for early discussions on methods of generating circularly polarized microwaves.

■ REFERENCES

(1) Pirandola, S.; Bardhan, B. R.; Gehring, T.; Weedbrook, C.; Lloyd, S. Advances in photonic quantum sensing. *Nat. Photonics* **2018**, *12*, 724−733.

(2) Schirhagl, R.; Chang, K.; Loretz, M.; Degen, C. L. Nitrogen-Vacancy Centers in Diamond: Nanoscale Sensors for Physics and Biology. *Annu. Rev. Phys. Chem.* **2014**, *65*, 83−105.

(3) Degen, C. L.; Reinhard, F.; Cappellaro, P. Quantum sensing. *Rev. Mod. Phys.* **2017**, *89*, No. 035002.

(4) Budker, D.; Romalis, M. Optical magnetometry. *Nat. Phys.* **2007**, *3*, 227−234.

(5) Romach, Y.; et al. Spectroscopy of Surface-Induced Noise Using Shallow Spins in Diamond. *Phys. Rev. Lett.* **2015**, *114*, No. 017601.

(6) Sangtawesin, S.; Dwyer, B. L.; Srinivasan, S.; Allred, J. J.; Rodgers, L. V.; De Greve, K.; Stacey, A.; Dontschuk, N.; O'Donnell, K. M.; Hu, D.; et al. Origins of Diamond Surface Noise Probed by Correlating Single-Spin Measurements with Surface Spectroscopy. *Physical Review X* **2019**, *9*, No. 031052.

(7) Azzam, S. I.; Parto, K.; Moody, G. Prospects and challenges of quantum emitters in 2D materials. *Appl. Phys. Lett.* **2021**, *118*, 240502.

(8) Ren, S.; Tan, Q.; Zhang, J. Review on the quantum emitters in two-dimensional materials. *Journal of Semiconductors* **2019**, *40*, No. 071903.

(9) Caldwell, J. D.; Aharonovich, I.; Cassabois, G.; Edgar, J. H.; Gil, B.; Basov, D. N. Photonics with hexagonal boron nitride. *Nature Reviews Materials* **2019**, *4*, 552−567.

(10) Kubanek, A. Coherent Quantum Emitters in Hexagonal Boron Nitride. *Advanced Quantum Technologies* **2022**, *5*, 2200009.

(11) Cassabois, G.; Valvin, P.; Gil, B. Hexagonal boron nitride is an indirect bandgap semiconductor. *Nat. Photonics* **2016**, *10*, 262−266.

(12) Kianinia, M.; et al.Robust Solid State Quantum System Operating at 800 K. *Conference on Lasers and Electro-Optics*; 2017; p JTu5A.24.

(13) Jungwirth, N. R.; Calderon, B.; Ji, Y.; Spencer, M. G.; Flatté, M. E.; Fuchs, G. D. Temperature Dependence of Wavelength Selectable Zero-Phonon Emission from Single Defects in Hexagonal Boron Nitride. *Nano Lett.* **2016**, *16*, 6052−6057.

(14) Xue, Y.; et al. Anomalous Pressure Characteristics of Defects in Hexagonal Boron Nitride Flakes. *ACS Nano* **2018**, *12*, 7127−7133.

(15) Gottscholl, A.; et al. Initialization and read-out of intrinsic spin defects in a van der Waals crystal at room temperature. *Nat. Mater.* **2020**, *19*, 540−545.

(16) Reimers, J. R.; et al. Photoluminescence, photophysics, and photochemistry of the V_B^- defect in hexagonal boron nitride. *Phys. Rev. B* **2020**, *102*, 144105.

(17) Chen, Y.; Quek, S. Y. Photophysical Characteristics of Boron Vacancy-Derived Defect Centers in Hexagonal Boron Nitride. *J. Phys. Chem. C* **2021**, *125*, 21791−21802.

(18) Ivády, V.; et al. Ab initio theory of the negatively charged boron vacancy qubit in hexagonal boron nitride. *npj Computational Materials* **2020**, *6*, 41.

(19) Gao, X.; et al. High-Contrast Plasmonic-Enhanced Shallow Spin Defects in Hexagonal Boron Nitride for Quantum Sensing. *Nano Lett.* **2021**, *21*, 7708−7714.

(20) Yu, P.; et al. Excited-State Spectroscopy of Spin Defects in Hexagonal Boron Nitride. *Nano Lett.* **2022**, *22*, 3545−3549.

(21) Mu, Z.; et al. Excited-State Optically Detected Magnetic Resonance of Spin Defects in Hexagonal Boron Nitride. *Phys. Rev. Lett.* **2022**, *128*, 216402.

(22) Mathur, N.; et al. Excited-state spin-resonance spectroscopy of V_B^- defect centers in hexagonal boron nitride. *Nat. Commun.* **2022**, *13*, 3233.

(23) Alegre, T. P. M.; Santori, C.; Medeiros-Ribeiro, G.; Beausoleil, R. G. Polarization-selective excitation of nitrogen vacancy centers in diamond. *Phys. Rev. B* **2007**, *76*, 165205.

(24) Yuan, H.; Yang, X.; Zhang, N.; Han, Z.; Xu, L.; Zhang, J.; Bian, G.; Fan, P.; Li, M.; Liu, Y. Frequency-Tunable and Circularly Polarized Microwave Resonator for Magnetic Sensing With NV Ensembles in Diamond. *IEEE Sensors Journal* **2020**, *20*, 8477−8482.

(25) Mrózek, M.; Mlynarczyk, J.; Rudnicki, D. S.; Gawlik, W. Circularly polarized microwaves for magnetic resonance study in the GHz range: Application to nitrogen-vacancy in diamonds. *Appl. Phys. Lett.* **2015**, *107*, No. 013505.

(26) Herrmann, J.; Appleton, M. A.; Sasaki, K.; Monnai, Y.; Teraji, T.; Itoh, K. M.; Abe, E. Polarization- and frequency-tunable microwave circuit for selective excitation of nitrogen-vacancy spins in diamond. *Appl. Phys. Lett.* **2016**, *109*, 183111.

(27) Yang, X.; Zhang, N.; Yuan, H.; Bian, G.; Fan, P.; Li, M. Microstrip-line resonator with broadband, circularly polarized, uniform microwave field for nitrogen vacancy center ensembles in diamond. *AIP Advances* **2019**, *9*, No. 075213.

(28) Yaroshenko, V.; et al. Circularly polarized microwave antenna for nitrogen vacancy centers in diamond. *Rev. Sci. Instrum.* **2020**, *91*, No. 035003.

(29) Zheng, H.; Xu, J.; Iwata, G. Z.; Lenz, T.; Michl, J.; Yavkin, B.; Nakamura, K.; Sumiya, H.; Ohshima, T.; Isoya, J.; Wrachtrup, J.; Wickenbrock, A.; Budker, D. Zero-Field Magnetometry Based on Nitrogen-Vacancy Ensembles in Diamond. *Phys. Rev. Appl.* **2019**, *11*, No. 064068.

(30) Pellet-Mary, C.; Perdriat, M.; Huillery, P.; Hétet, G. Relaxation Processes in Dipole-Coupled Nitrogen-Vacancy Centers in Zero Field: Application in Magnetometry. *Phys. Rev. Appl.* **2023**, *20*, No. 034050.

(31) Dhungel, O.; Lenz, T.; Omar, M.; Rebeirro, J. S.; Luu, M.-T.; Younesi, A. T.; Ulbricht, R.; Ivády, V.; Gali, A.; Wickenbrock, A.; Budker, D. Near zero-field microwave-free magnetometry with ensembles of nitrogen-vacancy centers in diamond. *Phys. Rev. B* **2024**, *109*, 224107.

(32) Riendeau, E. G.; Basso, L.; Mah, J. J.; Cong, R.; Sadi, M.; Henshaw, J.; Azizur-Rahman, K.; Jones, A.; Joshi, G.; Lilly, M. P.; Mounce, A. A. Quantum Instrumentation Control Kit−Defect Arbitrary Waveform Generator (QICK-DAWG): A Quantum Sensing Control Framework for Quantum Defects. 2023; https://arxiv.org/abs/2311.18253.

(33) Gao, X.; Vaidya, S.; Li, K.; Ju, P.; Jiang, B.; Xu, Z.; Llacsahuanga Allcca, A. E.; Shen, K.; Taniguchi, T.; Watanabe, K.; Bhave, S. A.; Chen, Y. P.; Ping, Y.; Li, T. Nuclear spin polarization and control in hexagonal boron nitride. *Nat. Mater.* **2022**, *21*, 1024−1028.

(34) Gracheva, I. N.; et al. Symmetry of the Hyperfine and Quadrupole Interactions of Boron Vacancies in a Hexagonal Boron Nitride. *J. Phys. Chem. C* **2023**, *127*, 3634−3639.

(35) Candido, D. R.; Flatté, M. E. Theory of spin center sensing of diffusion and other surface electric dynamics. *Phys. Rev. B* **2024**, *110*, 174450.

(36) Patel, R. N.; Fishman, R. E. K.; Huang, T.-Y.; Gusdorff, J. A.; Fehr, D. A.; Hopper, D. A.; Breitweiser, S. A.; Porat, B.; Flatté, M. E.; Bassett, L. C. Room Temperature Dynamics of an Optically Addressable Single Spin in Hexagonal Boron Nitride. *Nano Lett.* **2024**, *24*, 7623−7628.

(37) Candido, D. R.; Flatté, M. E. Interplay between charge and spin noise in the near-surface theory of decoherence and relaxation of C_{3v} symmetry qutrit spin-1 centers. *Phys. Rev. B* **2024**, *110*, No. 024419.

(38) Elko, M. J.; Hassenmayer, D. T.; Higgins, A. A.; Lenahan, P. M.; Flatté, M. E.; Fehr, D.; Craven, M. D.; Larsen, T. D. Near zero-field magnetoresistance and defects in gallium nitride pn junctions. *J. Vac. Sci. Technol. B* **2024**, *42*, No. 052205.

(39) Whitefield, B.; Toth, M.; Aharonovich, I.; Tetienne, J.-P.; Kianinia, M. Magnetic Field Sensitivity Optimization of Negatively

Charged Boron Vacancy Defects in hBN. *Advanced Quantum Technologies* **2025**, *8*, 2300118.

https://doi.org/10.1021/acs.nanolett.5c03056
Nano Lett. 2025, 25, 12067−12074